Composite Structures 351 (2025) 118613

Contents lists available at ScienceDirect

Composite Structures

journal homepage: www.elsevier.com/locate/compstruct

Fatigue delamination damage analysis in composite materials through a rule of mixtures approach

Alireza Taherzadeh-Fard [a,b,*], Sergio Jiménez [a,b], Alejandro Cornejo [a,b], Eugenio Oñate [a,b], Lucia Gratiela Barbu [a,b]

[a] Polytechnic University of Catalonia (UPC), Campus Nord, 08034 Barcelona, Spain
[b] International Center for Numerical Methods in Engineering (CIMNE), Campus Nord UPC, 08034 Barcelona, Spain

ARTICLE INFO

Keywords:
Rule of mixtures
Homogenization
Fatigue
Delamination
Composites
Finite element method

ABSTRACT

The present study investigates delamination damage initiation and propagation within a homogenization theory of mixtures, using the concept of virtual layers and virtual interfaces. It eliminates spatial discretization of layers, introducing a resultant damage variable to capture structure's bulk response under both monotonic and cyclic loads. Fatigue-induced deterioration is classified into sub-critical, critical, and over-critical stages based on interfacial stresses. Calibration is conducted employing the widely-available Wöhler curves for each loading mode independently. An advance-in-time strategy is included in the model to enhance the simulation speed. The reliability of the approach is assessed for crack initiation and propagation separately through standard test coupons, showing good correlation with experimental data in mode I, mode II, and mixed-mode loading conditions. Depending on the calibration procedure adopted, the model is applicable to a wide range of stress ratios. In addition, it could be integrated into any standard finite element framework using the desired number of elements through the thickness regardless of the physical amount of layers. This allows easy modification of stacking sequences or the number of layers within the constitutive law without mesh structure changes, facilitating simulation of large-scale composite laminates with minimal accuracy loss and reduced computational costs.

1. Introduction

Over the past recent years, composites have attracted much attention as the potential materials to be utilized in different industries including aerospace, automotive, marine, etc. [1,2], due to their superior mechanical properties such as corrosion and fatigue resistance, light weight, high strength and ease of transportation [3–6]. The multi-material nature of composite materials gives more freedom to engineers for designing purposes, however, this would lead to more damage mechanisms being engaged once these materials are under structural loading as well as more uncertainty in their bulk response due to manufacturing complexities [7–9]. Therefore, more advanced methodologies are required in studying the behavior of composites.

Damage mechanisms in composites are mainly comprised of intra-laminar and inter-laminar modes [10]. According to the complex nature of these damages and their interactions within the structure, simulation schemes have encountered challenges to compromise between accuracy and computational cost [11]. Among all degradation modes, interface failure or delamination has been of significant importance for its major effect on the strength and stiffness of the composite [12–15]. Indeed, laminated composites are fabricated through building up the in-plane fiber-reinforced laminae and are mainly expected to bear loading in the fiber direction. However, general loading conditions usually impose some through-the-thickness stresses to the composite, and can lead to failure of the matrix and initiation of the delamination phenomenon [16,17]. Debonding in the adjacent layers may not be catastrophic within the in-plane loading, nonetheless, for composites under out-of-plane loading or bending conditions, it could be fatal [18,19]. Prediction of this initiation and consequent propagation of the delamination crack has been associated with experimental full-scale testing procedures owing to the lack of enough knowledge and accurate numerical models, which, in turn, has made the design procedures to be highly expensive in terms of time and cost [20].

Fatigue delamination damage is mainly composed of three distinct stages of initiation, onset and propagation, and each of them has been characterized by different numerical approaches [21]. The initiation phase refers to the formation of the crack from an intact material and commonly originates from the imperfections formed during the

* Corresponding author at: Polytechnic University of Catalonia (UPC), Campus Nord, 08034 Barcelona, Spain.
E-mail addresses: alireza.taherzadeh.fard@upc.edu, atfard@cimne.upc.edu (A. Taherzadeh-Fard).

https://doi.org/10.1016/j.compstruct.2024.118613
Received 11 June 2024; Received in revised form 8 August 2024; Accepted 23 September 2024
Available online 27 September 2024

manufacturing process [11]. A common method to account for this stage is defining an initiation zone where damage could start appearing according to the models based on S-N curves [22,23]. In this way, S-N curves are formulated using experimentally-defined parameters and each mode is calibrated independently. Delamination onset, however, is defined as a visible increment in the crack through the medium from a crack starter. Although there is an unstable delamination crack propagation after crack initiation, crack onset is followed by a stable condition of crack extention [24]. Crack onset could be analyzed in a similar manner as initiation by considering fitting parameters to the experimental data [25], however this method lacks the ability to consider the mixed-mode and stress ratios.

Linear elastic fracture mechanics (LEFM) is a widely-used approach in simulating the fatigue crack in the propagation phase [26,27]. These models mainly employ any forms of the Paris law to make a connection between the crack growth and the energy release rate (ERR) [11]. Therefore, other methods should also be incorporated within this formulation to calculate the energy release rate or the stress intensity factor such as Virtual Crack Closure Technique (VCCT) [8,28–30], virtual crack extension [31,32], or crack surface displacement extrapolation methods [33]. Despite this, LEFM based models suffer from several problems such as the inability to be used in hybrid composites [34] or failure to initiate the fatigue crack within a pristine material [24].

Cyclic Cohesive Zone Method (CCZM) can also be used to simulate fatigue crack in composites which is based on defining a traction-separation law for damage evolution within the interface [23,35–39]. Based on how the cyclic load effects are taken into account, two different methods of hysteresis loop and envelope load damage models have been considered [40]. Hysteresis loop damage models degrade the strength and the stiffness within a cycle-by-cycle algorithm and are well suited for low-cycle fatigue regime [41]. Nevertheless, calibration of the parameters is considered to be a highly challenging task [40]. Envelope load damage models, on the other side, utilize jumping strategies combined with the Paris law to evolve delamination damage within the interface. This formulation could be beneficial in the high-cycle fatigue regime and is capable of considering different factors such as mode mix and stress ratios. However, implementing Paris law within the cohesive framework can be complex [42], and linking the damage variable to the traction-separation formulations is not straightforward [20]. In addition, it is not clear if the Paris law should be considered as a material property or rather a problem dependent variable. Consequently, fatigue delamination damage models that are not based on the Paris law are highly valuable.

Moreover, cohesive zone methods have several shortcomings. Mainly since they are dependent on the definition of an interface medium, crack path should be known a priori [43]. Additionally, incorporating interface elements within all interfaces would be a challenging task especially in composites with large number of layers. Since CCZMs are dependent on the definition of a traction-separation law with an initial linear part, they could manipulate the bulk response of the structure in its elastic region when there is not damage evolved within the interface [44]. Selection of the slope in CCZM linear part is also *ad-hoc* and requires a tuning process [45,46].

Recently, a continuum mechanics based fatigue model has been proposed by unifying different phenomena such as damage, plasticity, viscosity and temperature effects [47], and has been improved in other applications as well [48,49]. Indeed, the formulation triggers strength and stiffness deterioration once a specific stress criterion is satisfied. The degradation is accounted for by a damage-type constitutive law, while being sensitive to the cyclic loads through a fatigue reduction factor [50]. The factor also affects the fracture energy so that an energy dissipation is introduced to the model as a result of the cyclic loading. Model parameters are calibrated by using curve fitting to the common S-N curves. The model is expected to be applicable in a wide spectrum of fatigue scenarios while being capable of capturing both damage initiation and propagation over different amount of stress ratios.

In the current study, a homogenization theory of mixtures has been presented to model fatigue delamination damage response in laminated composites. The work is based on a previous research by the authors [51] where loading conditions were limited to the monotonic regime. Rather than considering cohesive elements at each interface, the proposed model employs a homogenized medium where there is no need to explicitly discretize composite layers, which could significantly facilitate the pre-processing stage as well as the optimization of the design process, since no re-meshing is required when the internal configuration of the composite changes. This is even more pronounced when modeling composites with large number of layers by accounting the number of elements needed through the thickness irrespective of the actual number of layers. The cyclic loading effect is introduced to the formulation by defining a fatigue reduction function which could be calibrated according to the common S-N curves for mode I and mode II, independently. Delamination damage effect, in both contexts of crack initiation and propagation, is reflected to the adjacent virtual bulk layers so that the bulk response of the structure is accurately reproduced, while not imposing any limitations on the constitutive law used for each layer. Therefore, in addition to the inter-layer damages, there is the possibility of intera-layer mechanical phenomena such as damage and plasticity. Since the *ad-hoc* interface penalty stiffness concept is eliminated from the formulation, structural response will no longer be manipulated in the elastic regime. The proposed model is compatible with any finite element code and is considered to be well-suited for simulating fatigue delamination in large-scale composites while maintaining the accuracy within an acceptable range.

2. Mathematical formulation

2.1. Preliminary concepts

In this section, some introductory information regarding the underlying rule of mixtures method and interfacial stresses is provided. The reader is referred to the previous work [51] for a complete description and fundamental hypotheses.

Composite laminates are mainly composed of a specific number of fiber reinforced laminae oriented at different directions. Trusdell and Toupin [52] firstly presented a method to unify all layers' behavior through a homogenization theory. Later on, the method has been developed by other researchers as well [53,54]. It is mainly based on the assumption that strains experienced by all laminae are the same whilst the stress of the composite is obtained by taking a super-position of the stress in each laminae according to its volumetric participation, i.e.:

$$\boldsymbol{\varepsilon}_1 = \boldsymbol{\varepsilon}_2 = \cdots = \boldsymbol{\varepsilon}_n \tag{1}$$

$$\boldsymbol{\sigma} = \sum_{i=1}^{n} (k_i \cdot \boldsymbol{\sigma}_i) \tag{2}$$

where $\boldsymbol{\varepsilon}_i$, k_i and $\boldsymbol{\sigma}_i$ are the strain tensor, volumetric participation and the stress tensor of the ith layer, respectively. From the homogenization point of view, the composite is made up of virtual bulk layers and virtual interfaces, as presented in Fig. 1, in a way that the response of the structure is reproduced correctly in the macro scale.

The first step in formulating the delamination is to prepare a foundation to calculate interfacial stresses. Since free edge effects are not accounted for in the homogenized medium, a straightforward averaging scheme is employed to obtain stresses at the interfaces, as follows:

$$\boldsymbol{\sigma}_i^{interface} = \frac{\boldsymbol{\sigma}_i^{bulk} + \boldsymbol{\sigma}_{i-1}^{bulk}}{2} \tag{3}$$

where $\boldsymbol{\sigma}_i^{interface}$ is the interfacial stress tensor at the ith interface while $\boldsymbol{\sigma}_i^{bulk}$ is the bulk layer stress tensor at the ith layer.

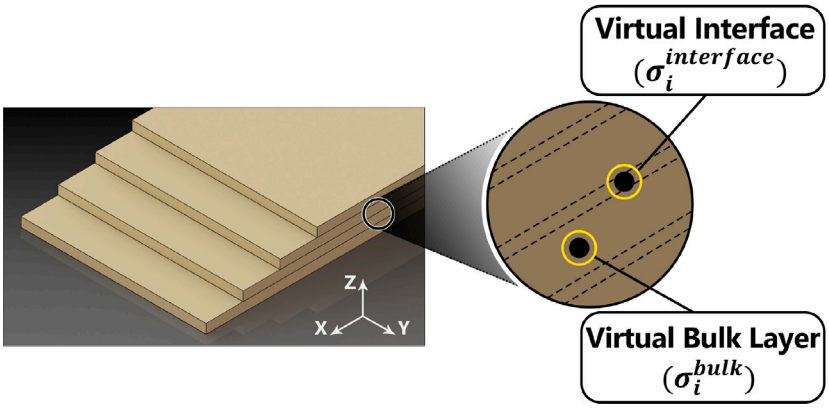

Fig. 1. Virtual bulk layers and virtual interfaces through the homogenized medium [51].

According to Balzani et al. [55], delamination is driven by a normal stress component acting perpendicular to the delamination plane and two shear stress components acting on the delamination plane. Considering the coordinate system presented in Fig. 1, two equivalent stresses are calculated to be fed into the delamination damage model for mode I and mode II loadings:

$$\sigma_{n,i}^{interface} = \left\langle \sigma_{zz,i}^{interface} \right\rangle \tag{4}$$

$$\sigma_{s,i}^{interface} = \sqrt{(\sigma_{xz,i}^{interface})^2 + (\sigma_{yz,i}^{interface})^2} \tag{5}$$

where $\sigma_{n,i}^{interface}$ and $\sigma_{s,i}^{interface}$ are the interfacial equivalent normal and shear stresses at the ith interface. $\langle \bullet \rangle$ are the Macaulay brackets to prevent damage evolution in normal compression loads [51].

2.2. Fatigue delamination damage evolution

In order to accumulate the fatigue effect into the current delamination formulation, a similar scheme to that described in [49] is adopted here. To this end, the failure indicators $F_{n,i}$ and $F_{s,i}$ previously developed at each interface i in [51] are modified by a *fatigue reduction function* (f^{red}) as below:

$$F_{n,i} = \frac{\sigma_{n,i}^{interface}}{f_{n,i}^{red}(N_{n,i}^{c}, R_{n,i}, S_{n,i}^{max})} - \sigma_{n,th,i}^{interface} > 0 \tag{6}$$

$$F_{s,i} = \frac{\sigma_{s,i}^{interface}}{f_{s,i}^{red}(N_{s,i}^{c}, R_{s,i}, S_{s,i}^{max})} - \sigma_{s,th,i}^{interface} > 0 \tag{7}$$

where subscriptions n and s refer to normal mode I and shear mode II loadings, respectively. $\sigma_{n,th,i}^{interface}$ and $\sigma_{s,th,i}^{interface}$ are historical variables of the interface threshold stress in mode I and mode II, and their initial value would consider to be normal and shear interface strengths, respectively. These values will be updated at each step to the maximum historical normal ($\sigma_{n,i}^{interface}$) and shear ($\sigma_{s,i}^{interface}$) uni-axial stresses obtained previously. Once inequalities (6) and (7) are satisfied, the crack is permitted to grow.

$f^{red}(N_{m,i}^{c}, R_{m,i}, S_{m,i}^{max})$ is introduced to the failure indicators to take the cyclic load effects into account by amplifying the stress state. Its value ranges from 1, indicating no cyclic load effect, down to 0 at the asymptote. According to the fatigue crack propagation through the interface, which is shown in Fig. 2, three different stages could be considered at each integration point, whilst each stage requires specific formulation for f^{red}, as described in the following.

2.2.1. Sub-critical fatigue stage

Once fatigue crack initiates and starts propagating, there are some areas in the far-field where the maximum cyclic stress at the interface (S^{max}) is below the fatigue limit, S_{th}, at a specific stress ratio, $R = S^{min}/S^{max}$, matching the blue area in Fig. 2(a). An element located in this area (black dashed strip) should not experience any cyclic load effects, and hence, the fatigue related quantities will be maintained in their initial values, as below:

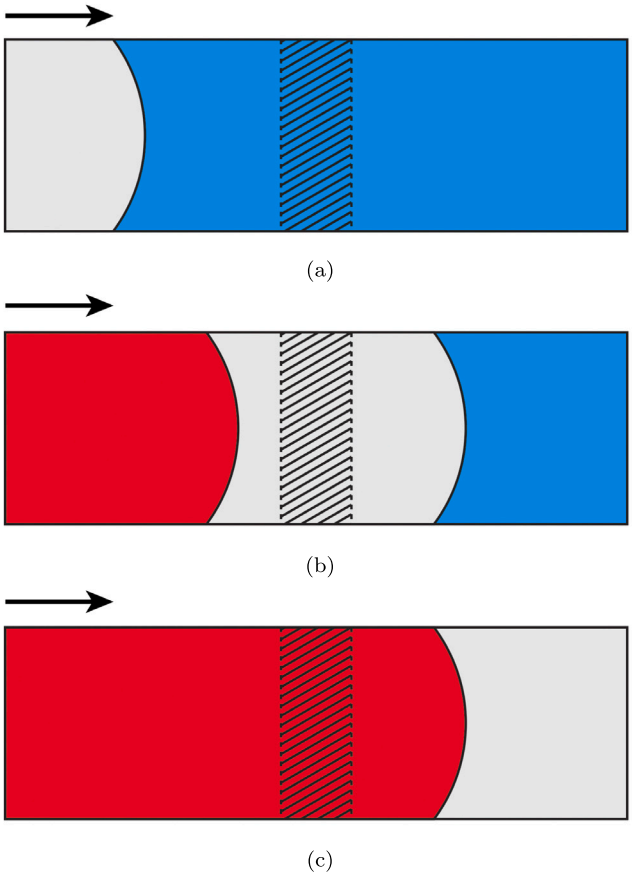

Fig. 2. Different stages experienced by a band of elements in (a) Sub-critical (blue), (b) Critical (gray), and (c) Over-critical (red) regions as fatigue crack propagates in the direction illustrated by arrows.

$$f_{m,i}^{red} = 1 \tag{8}$$

$$N_{m,i}^{c} = 0 \tag{9}$$

where $N_{m,i}^{c}$ is the number of cycles at the ith interface and m stands for n or s in normal and shear loadings, respectively. As the crack

propagates, the black dashed area becomes closer to the crack tip and the maximum cyclic stress levels will increase, which necessitates a different description for the f^{red}.

2.2.2. Critical fatigue stage

When a specific element experiences stresses greater than the fatigue limit and below the static strength, the cyclic load effects should be considered through f^{red}. This situation is observed by the elements within the shaded area in the gray region in Fig. 2(b), where variation of f^{red} could trigger two kinds of non-linearity. The first one is the gradual amplifying of the interfacial stresses (or literally, the gradual decrease of the strength) as a result of the f^{red} evolution when N^c is growing. The second one, which is a consequence of the first one, is the rapid propagation of the crack once N^c reaches the critical number of cycles (N^f) and inequalities (6) and (7) are met.

The definition of the f^{red} function can be done based on either G-N (energy release rate vs. number of cycles) or S-N (Interfacial stress vs. number of cycles) diagrams. Indeed, the model in this study has originated from the high-cycle fatigue (HCF) formulation presented by Oller et al. [47], which has been developed for metals based on S-N curves. Successful implementation and satisfactory results of this formulation in HCF regime [49,56] triggered the idea of applying the same approach in composite materials [57]. Therefore, although calibrating the model based on G-N curves seems to be more applicable as for more availability of these curves for composite materials, present formulation has been established based on the stress curves. Supporting this approach, there are recently-published papers where S-N curves have been employed, and a calibration process has been conducted accordingly to model the delamination propagation in laminated composites [58,59]. This may indicate the potential of the S-N curves in this context. Moreover, according to [42], some inter-connections could be established between the common Paris law (da/dN vs. G) and the S-N curve in composites. This would be an asset for the current approach in this study, since there is the potential to feed the Paris law to the model and make calibrations accordingly. This issue has not been addressed in current study, and would be a matter of future investigations.

Definition of f^{red} for the interface is conducted through a fitting procedure with respect to the common S-N surfaces of the type [49]:

$$S_{m,i}(R_{m,i}, N^c_{m,i}) = S^{th}_{m,i}(R_{m,i}) + \left(S^u_{m,i} - S^{th}_{m,i}(R_{m,i})\right) \cdot \exp\{-\alpha^t_{m,i}(R_{m,i}) \cdot \left(\log N^c_{m,i}\right)^{\beta^f_{m,i}}\} \tag{10}$$

$R_{m,i}$ and $S^u_{m,i}$ being the stress ratio and static strength for mode m at the ith interface, respectively. $S^{th}_{m,i}(R_{m,i})$ is the fatigue limit at the ith interface:

$$\begin{cases} \text{if } |R| \le 1 \Rightarrow S^{th}_{m,i}(R_{m,i}) = S^e_{m,i} + \left(S^u_{m,i} - S^e_{m,i}\right) \cdot \left(\dfrac{1+R_{m,i}}{2}\right)^{S^{R1}_{m,i}} \\ \text{if } |R| > 1 \Rightarrow S^{th}_{m,i}(R_{m,i}) = S^e_{m,i} + \left(S^u_{m,i} - S^e_{m,i}\right) \cdot \left(\dfrac{1+R_{m,i}}{2R_{m,i}}\right)^{S^{R2}_{m,i}} \end{cases} \tag{11}$$

where $S^e_{m,i}$ is the fatigue limit at $R_{m,i} = -1$. $\alpha^t_{m,i}(R_{m,i})$ is a parameter which depends on the state of loading as described below:

$$\begin{cases} \text{if } |R| \le 1 \Rightarrow \alpha^t_{m,i}(R_{m,i}) = \alpha^f_{m,i} + \left(\dfrac{1+R_{m,i}}{2}\right) \cdot AUX^{R1}_{m,i} \\ \text{if } |R| > 1 \Rightarrow \alpha^t_{m,i}(R_{m,i}) = \alpha^f_{m,i} - \left(\dfrac{1+R_{m,i}}{2R_{m,i}}\right) \cdot AUX^{R2}_{m,i} \end{cases} \tag{12}$$

$S^{R1}_{m,i}$, $S^{R2}_{m,i}$, $\alpha^f_{m,i}$, $\beta^f_{m,i}$, $AUX^{R1}_{m,i}$ and $AUX^{R2}_{m,i}$ are material properties and could be calibrated at each interface i for each mode of loading m. The more Wöhler diagrams in different stress ratios are considered in the calibration, the more accurate description of the S-N surface will be obtained in a wide spectrum of stress ratios.

Once S-N surface has been defined and formulated, an expression could be proposed for fatigue reduction function in the form

$$f^{red}_{m,i}(N^c_{m,i}, R_{m,i}, S^{max}_{m,i}) = \exp\left[\frac{\ln\left(S^{max}_{m,i}/S_{m,u,i}\right)}{\left(\log N^f_{m,i}\right)^{\left(\beta^f_{m,i}\right)^2}} \left(\log N^c_{m,i}\right)^{\left(\beta^f_{m,i}\right)^2}\right]. \tag{13}$$

According to Fig. 3, when a cyclic load at a specific $S^{max}_{m,i}$ is applied within the critical fatigue stage, a unique $f^{red}_{m,i}$ function could be found which intersects the normalized S-N curve at $N^f_{m,i}$. $N^f_{m,i}$ is a critical quantity which will be used in the next sessions for the jumping strategy. Its value could be obtained by setting $N^c_{m,i} = N^f_{m,i}$ in Eq. (13), then equating the outcome to the result from Eq. (10):

$$N^f_{m,i}(R_{m,i}, S^{max}_{m,i}) = 10^{\left[\left[-\frac{1}{\alpha^t_{m,i}(R_{m,i})} \cdot \ln\left(\frac{S^{max}_{m,i} - S^{th}_{m,i}(R_{m,i})}{S^u_{m,i} - S^{th}_{m,i}(R_{m,i})}\right)\right]^{\frac{1}{\beta^f_{m,i}}}\right]} \tag{14}$$

Generally, as long as $N^c_{m,i} < N^f_{m,i}$, the non-linearities would be strength deterioration and fracture energy dissipation, according to the $f^{red}_{m,i}$ evolution. Once $N^c_{m,i} \ge N^f_{m,i}$, in addition to the strength, the stiffness will be degrading as well, which corresponds to a rapid failure process in the integration point level according to inequalities (6) and (7).

Matlab software [60] is employed in the fitting process and to find proper values for the engaged parameters. To this end, the more experimental data is provided, the wider the reliable region will be in terms of stress ratio, R, and maximum stress, S^{max}. In other words, the model should be well-prepared prior to simulations to be able to treat as close as possible to the provided experimental Wöhler surface. In this way, the formulation could be applicable in different loading scenarios.

2.2.3. Over-critical fatigue stage

Over-critical fatigue stage refers to the region where predictive stresses are greater than the static strength of the material. This situation happens as the crack propagates through the interface and the crack opening increases cycle-by-cycle, as is the case for the elements located within the red region in Fig. 2(c). The irreversible degradation process of the interface has to be reflected in the $f^{red}_{m,i}$ quantity. However, a different formulation than the one for the critical region should be employed. Consequently, a similar approach to [61] is adopted by considering a fatigue-induced degradation as:

$$\frac{\mathrm{d}f^{red}_{m,i}}{\mathrm{d}N^c_{m,i}} = -\frac{1}{\gamma_{m,i}}\left(N^c_{m,i}\right)^{-\eta_{m,i}} \tag{15}$$

where $\gamma_{m,i}$ and $\eta_{m,i}$ are interface parameters describing the rate of degradation, and their value could be obtained according to the experimental campaign.

2.3. Fatigue delamination damage effect

Once the failure criteria in Eqs. (6) and/or (7) are satisfied – either by evolution of $f^{red}_{m,i}$ or increasing the $\sigma^{interface}_{m,i}$ – the damage variable for each mode m and interface i is calculated independently according to an exponential softening law [51,62]:

$$d_{m,i} = 1 - \frac{\sigma^{0,th}_{m,i}}{\sigma^{interface}_{m,i}} \exp\left[A_{m,i}\left(1 - \frac{\sigma^{interface}_{m,i}}{\sigma^{0,th}_{m,i}}\right)\right] \tag{16}$$

where

$$A_{m,i} = \frac{1}{\dfrac{C_{m,i}G_{m,i}}{(\sigma^{0,th}_{m,i})^2 l_c} - \frac{1}{2}} \tag{17}$$

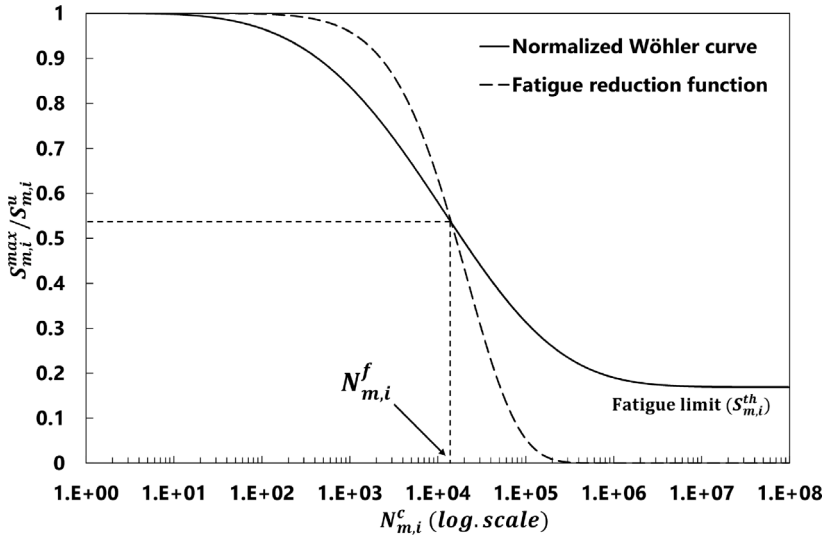

Fig. 3. Normalized Wöhler and fatigue reduction function curves in a general loading state.

$\sigma^{0,th}_{m,i}$, $C_{m,i}$, $G_{m,i}$, and l_c being either mode I or mode II interfacial strength, modulus, fracture toughness and characteristic length, respectively. As explained in previous work [51], transverse Young's and transverse shear moduli of the bulk layers are considered as the interfacial normal and shear moduli, whilst half of the element length is regarded as the characteristic length.

Since there is not dedicated medium for the interface layer, delamination damage effects should be properly reflected in the virtual bulk layers so that the behavior of the structure at macro-scale is well-captured. To this end, each bulk layer is affected by two maximum normal (d_n) and shear (d_n) damages as below [51]:

$$\sigma^{bulk,\,d}_{zz,i} = (1 - \max[d_{n,i}, d_{n,i-1}])\sigma^{bulk}_{zz,i} \tag{18}$$

$$\sigma^{bulk,\,d}_{xz,i} = (1 - \max[d_{s,i}, d_{s,i-1}])(1 - \max[d_{n,i}, d_{n,i-1}])\sigma^{bulk}_{xz,i} \tag{19}$$

$$\sigma^{bulk,\,d}_{yz,i} = (1 - \max[d_{s,i}, d_{s,i-1}])(1 - \max[d_{n,i}, d_{n,i-1}])\sigma^{bulk}_{yz,i} \tag{20}$$

where $(\sigma^{bulk}_{zz,i}, \sigma^{bulk}_{xz,i}, \sigma^{bulk}_{yz,i})$ are predictive stresses acting on the delamination plane. They would be considered as the integrated stresses ($\sigma^{bulk,\,d}_{zz,i}$, $\sigma^{bulk,\,d}_{xz,i}$ and $\sigma^{bulk,\,d}_{yz,i}$) once affected by the delamination damage. All other stress components remain unaffected in terms of the delamination phenomenon [55].

To illustrate the performance of the presented formulation in different scenarios, two types of loading conditions are schematically presented in Fig. 4. In Fig. 4(a), a cyclic load is applied within the critical fatigue stage followed by a monotonic loading part. The model is expected to activate the first non-linearity as the result of the $f^{red}_{m,i}$ evolution and decrease the interface strength accordingly. However, in Fig. 4(b), a monotonic load is applied followed by a cyclic load within the over-critical fatigue region. As it is obvious, the response follows the same path as in the monotonic loading regime in the first cycle, whilst a progressive degradation in both strength and stiffness happens once the load is switched to a cyclic one.

2.4. Advance-in-time strategy

According to Eqs. (13) and (15), the fatigue delamination method developed in the present study employs three independent quantities of $N^c_{m,i}$, $R_{m,i}$ and $S^{max}_{m,i}$ in the critical regime, and one quantity of $N^c_{m,i}$ in the over-critical region to identify the state of the sample within the cyclic loading. Although $R_{m,i}$ and $S^{max}_{m,i}$ are computed at each step and are completely dependent on the exerted external loads, $N^c_{m,i}$ is a continuous variable in the time domain and requires progressive growth within the simulation. This could be problematic, specifically in high-cycle fatigue situations due to the high computational cost associated. Therefore, a procedure should be considered to skip a number of cycles while compensating for its effects within the formulation to reduce the computational costs.

To this end, an advance-in-time (AIT) strategy is considered once stable conditions are obtained in terms of the cyclic loading exerted. The method is based on the jump strategy proposed in [49,50,57,63], however it is enhanced to account for two different loading mode conditions. Indeed, previous version of the AIT method has been presented for isotropic materials where the distinction between mode I or mode II loadings was not necessary. In the case of the numerical framework proposed in this study, that is no longer the case, a method is developed to identify to most critical mode of loading, and the jump is set up accordingly.

Let us consider that mode I and mode II loadings are activated in the critical fatigue region, as shown schematically in Fig. 5. To maintain generality, loading modes are referred to as modes k and l. Depending on the time when either mode has reached the critical fatigue region, the number of cycles before jump (N^c_i) could be different, since in the sub-critical fatigue stage cycles are not counted according to Eq. (9). On the other hand, the required number of cycles to reach the damage initiation conditions could be obtained using Eq. (14) for each loading mode, independently. It would be reasonable to employ the most critical loading mode in terms of the distance to the damage initiation conditions, so that the other mode remains in the allowable S-N area after the jump. As a result, the loading mode with the minimum amount of $N^f - N^c$ will be fed into the AIT strategy.

Other combinations of loading modes are still possible, where the selection of the mode for the AIT strategy is quite straightforward. Within all other possibilities, loading mode in the over-critical fatigue stage would be selected for AIT strategy compared to the one in the critical fatigue stage, while critical fatigue stage will be prioritized over the sub-critical fatigue region.

The jump is expected to occur once stable conditions are reached in the stress state. While the crack is propagating, the maximum cyclic stress is continuously evolving at each integration point. In this way, stability condition means a plateau in the damage and stress evolution which could be monitored employing two indicators:

$$\varphi_{m,i} = \left| \frac{S^{max}_{m,i,j+1} - S^{max}_{m,i,j}}{S^{max}_{m,i,j+1}} \right| < tolerance \tag{21}$$

$$\psi_{m,i} = \left| \frac{R_{m,i,j+1} - R_{m,i,j}}{R_{m,i,j+1}} \right| < tolerance \tag{22}$$

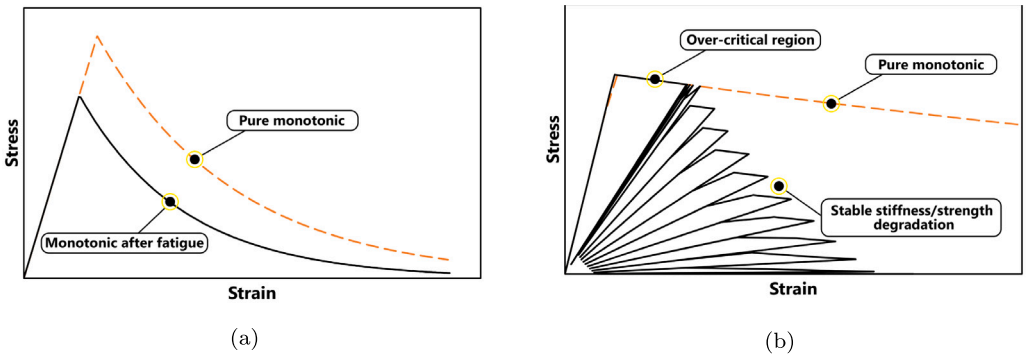

Fig. 4. Model performance in two different loading scenarios: (a) cyclic load followed by a monotonic tension within the critical area and (b) monotonic tension followed by a cyclic loading within the over-critical region.

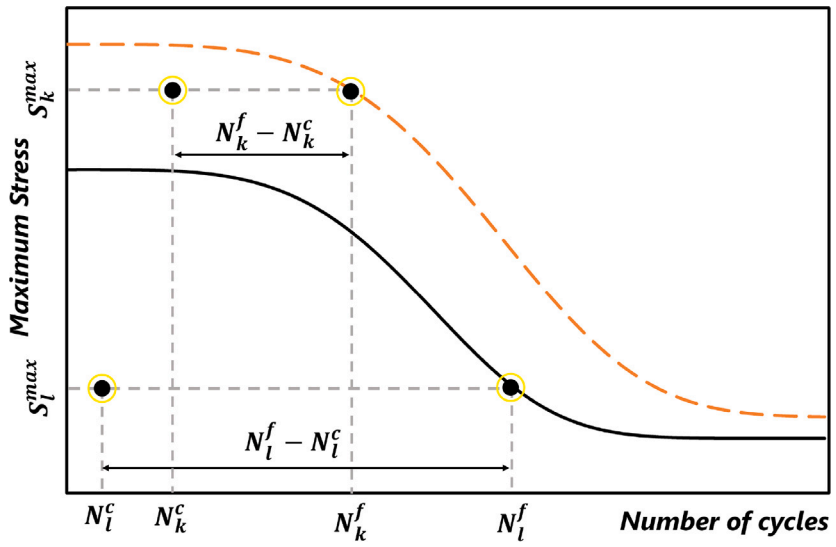

Fig. 5. Criticality level of two different loading modes in terms of the number of remaining cycles to failure.

$\varphi_{m,i}$ and $\psi_{m,i}$ being maximum stress and stress ratio stabilization norms, while $S_{m,i,j}^{max}$ and $R_{m,i,j}$ being the maximum stress and the stress ratio of mode m, interface i and time step j, respectively. Once stability conditions in Eqs. (21) and (22) are satisfied, the process time as well as the number of cycles at each integration point will be updated, and the $f_{m,i}^{red}$ is calculated based on the newly-obtained number of cycles.

3. Numerical examples and results

The potential of the proposed model is studied in this section through different loading scenarios in both damage initiation and damage propagation regimes. Unidirectional carbon fiber/epoxy prepreg (IM7/8552) properties have been employed, and the validations are conducted on this composite in all fatigue crack evolution assessments.

It should be noted that, in the current study, the effect of fiber bridging has not been considered in the simulations. Indeed, the presented fatigue model acts in an integration-point-wise approach, where all the calculations are conducted at each Gauss-point within the finite element model. This implies that the basis of the fatigue model in current assessment is a local framework. However, taking into account the bridging effect necessitates additional information regarding the extent of delamination damage crack, since the R-curve phenomenon depends upon the length of the crack propagated. To this end, non-local methods should be taken into account to efficiently consider the fiber bridging effects. Ignorance of the R-curve effect would not impose any problems for the damage initiation stage, however, damage propagation would be affected by this assumption. It will be demonstrated that in the absence of the fiber bridging effects, the results still fall within an acceptable range of the experimental data.

The presented fatigue formulation is implemented through the open-source code Kratos Multi-physics [64,65]. Geometry and mesh generation has been conducted utilizing pre and post processing software GiD [66].

3.1. Constitutive law parameters calibration

As it has been mentioned in Section 2.2.2, a Matlab fitting algorithm is employed to calibrate the fatigue parameters of the model. To this end, Wöhler diagrams of the interface in each loading mode is required to effectively characterize the fatigue delamination behavior. Transverse tension [18,67] and shear [22,68] fatigue tests have been conducted on the IM7/8552 carbon/epoxy composite at different stress ratios ($R_{m,i}$) and stress levels ($S_{m,i}^{max}$) until the crack is initiated within the interface. The resulted experimental S-N diagrams are utilized to fit a curve in the form of Eq. (10) for each mode I and mode II. The experimental Wöhler curves along with the calibrated model responses are presented in Fig. 6.

Tables 1 and 2 present the material properties as well as the obtained values for the calibrated interfacial parameters, respectively. These properties will be used within the simulations in the following sections for both fatigue damage initiation and propagation regimes. Since all the simulations are conducted at $R_{m,i} < 1$, there is no need to calibrate $S_{m,i}^{R2}$ and $AUX_{m,i}^{R2}$ parameters.

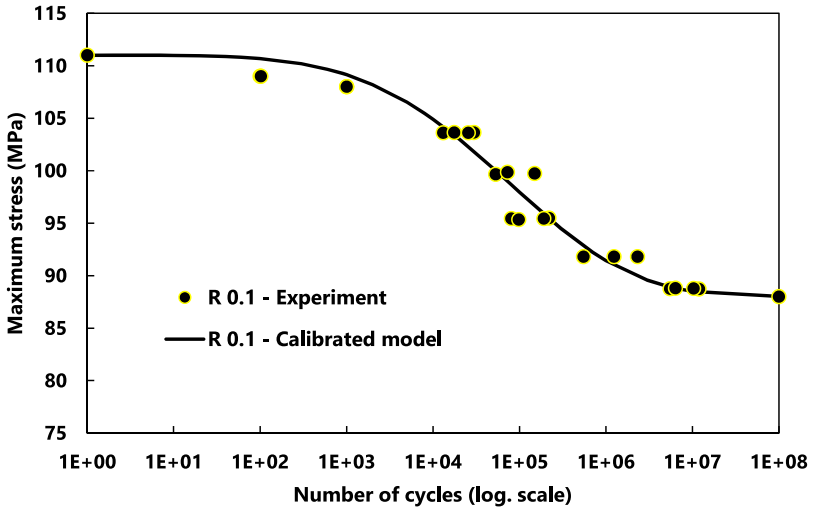

(a)

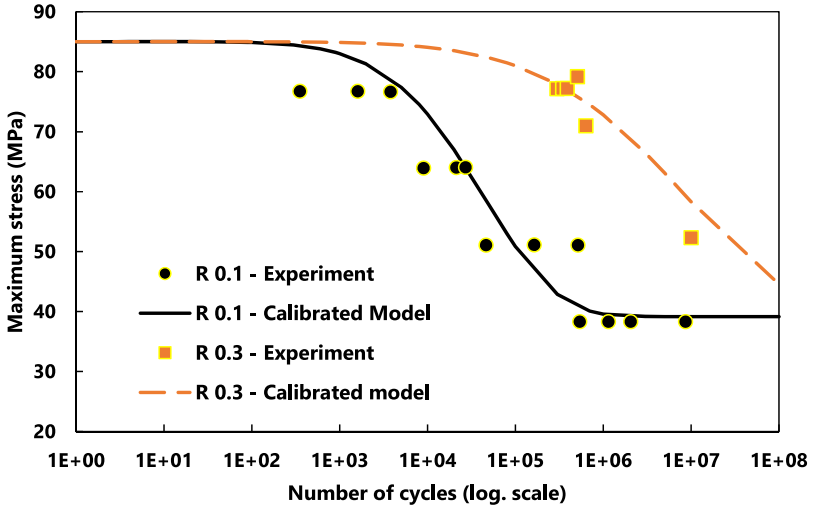

(b)

Fig. 6. Fatigue material model calibration in (a) transverse normal (mode I) and (b) shear (mode II) configurations compared to the experimental data [18,68].

Table 1
Mechanical properties of the IM7/8552 carbon/epoxy prepreg [22].

Mechanical property	Value
E_1 [GPa]	161
$E_2 = E_3$ [GPa]	11.4
$G_{12} = G_{13}$ [GPa]	5.17
G_{23} [GPa]	3.98
$\nu_{12} = \nu_{13}$	0.32
ν_{23}	0.43

Table 2
Calibrated interfacial fatigue parameters for modes I and II [68].

Interface property	Normal load (Mode I)	Shear load (Mode II)
Energy release rate (G) [J/m^2]	212	600
Interfacial strength (σ^0_{th}) [MPa]	111	85
Interfacial modulus (C) [GPa]	11.4	5.17
S^e [MPa]	87.7	39.1
S^{R1} [MPa]	48.88	55.81
α^f	2.14e−3	1.69e−4
β^f	4.49	6.71
AUX^{R1}	−2.80e−3	−2.58e−4
γ	25	30
η	0.72	0.72

3.2. Fatigue delamination damage initiation assessment

In order to investigate the model capability to initiate fatigue crack in an undamaged medium, two standard tests have been employed in each loading mode, as illustrated in Fig. 7. Three-point bending test is utilized to initiate the fatigue crack in mode I loading. To this end, a central displacement is cycled with a frequency of 1 Hz while the two ends of the cantilever beam are set to be fixed through the whole width (w = 6.35 mm), as shown in Fig. 7(a).

Cyclic displacement domains are chosen in a way that they produce maximum normal stresses of 90, 93, 97, 101, and 105.5 MPa within the central region. Carbon fibers are aligned in the loading direction and in 90° angle with respect to the longitudinal direction. Hexahedron elements with the size of 0.1 mm are employed in the central region, where the crack is expected to initiate, and coarse meshes are opted for the far-field area. The cycle is defined to induce 0.1 stress ratio states according to the experimental procedure, and the results are presented in Fig. 8 compared against the experimental data. Within the experimental tests, specimens in both standard tests fail catastrophically once damage has initiated, which allows simple detection of the damage

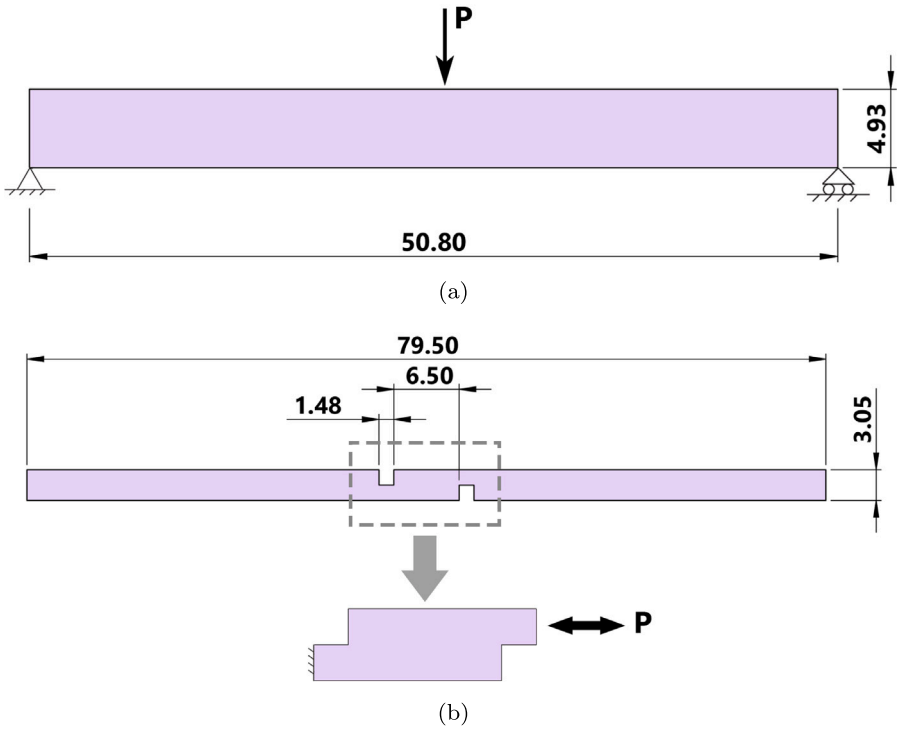

Fig. 7. Schematic view of (a) three-point bending and (b) double-notched shear tests under cyclic load (dimensions in millimeters).

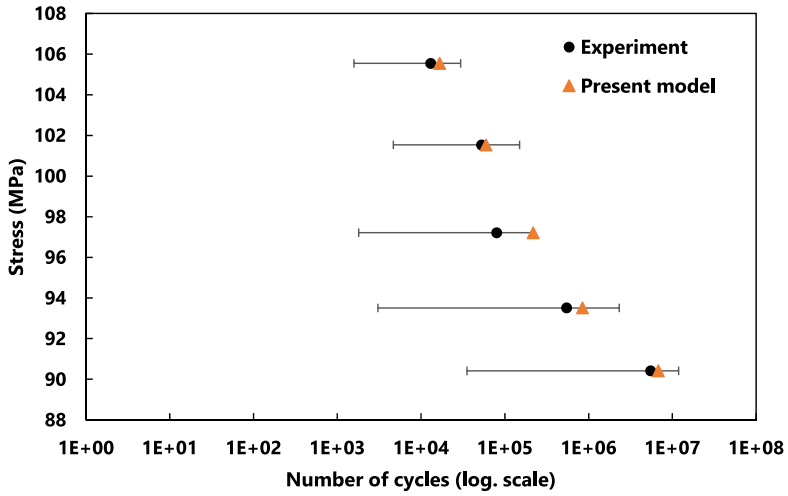

Fig. 8. Initiation of the fatigue crack in the three-point bending configuration under mode I loading compared with the experimental data at $R = 0.1$ [18,23].

onset. In the numerical framework, however, the necessary number of cycles to initiate the delamination damage is calculated according to Eq. (14). This value has been considered as the crack initiation point within the simulations.

As it can be observed, the model captures the crack initiation cycle fairly well at each stress level, and the numerical output lies within the experimental scatter region. In the simulations, fatigue crack propagates catastrophically once it has been initiated, which aligns with the experimental findings [18,23]. In Fig. 9, the crack initiation step and its complete propagation is presented at the stress level of 97 MPa. Through the simulation, a deactivation algorithm is employed to erase fully damaged elements so that the model converges more easily.

Validating the performance of the model in mode I loading, it would be valuable to check its applicability in shear mode as well. Therefore, experimental double-notched shear test results are utilized for running pure mode II simulations [68]. The configuration of the test is shown in Fig. 7(b) where carbon fibers are aligned in the longitudinal direction. A cyclic axial displacement is applied to one end through the whole width (w = 12.7 mm) so that it produces shear stresses at the central part. From the numerical point of view, considering solely the central part would be enough to run the simulations. Two stress ratios of 0.1 and 0.3 are used along with a cyclic load of 1 Hz. The element size and type are the same as in the three-point bending test. Fig. 10 summarizes the numerical and experimental results.

The model output for mode II loading shows a good agreement with the experimental results. This indicates that the proposed formulation would be able to deal with the crack initiation phenomenon in both mode I and mode II loading conditions in an accurate manner. The next stage is assessing the performance of the model in the propagation regime, which will be discussed in the following section.

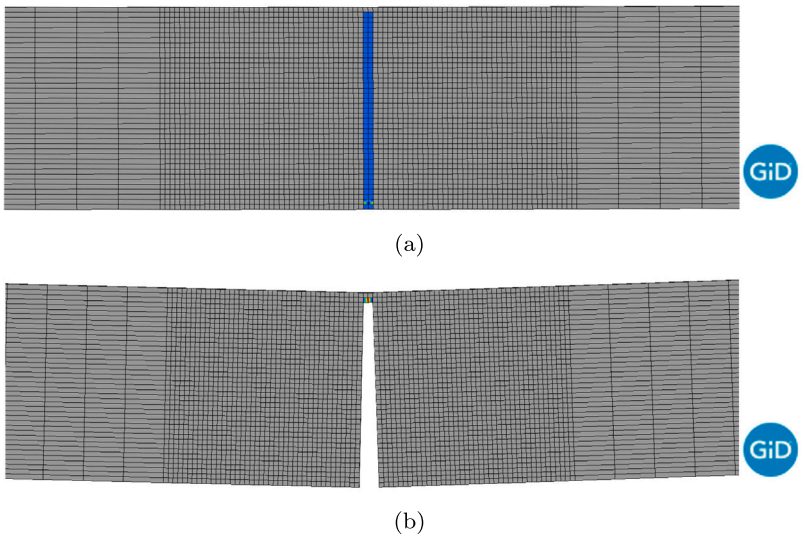

Fig. 9. Three-point bending fatigue simulations in the stress level of 97 MPa in (a) initiation stage at $N^c = 218\,964$ and (b) complete failure at $N^c = 218\,986$.

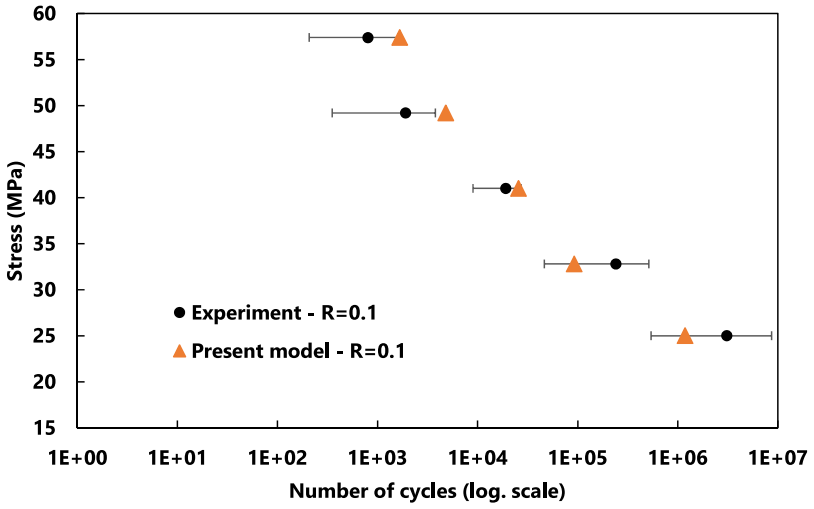

Fig. 10. Initiation of the fatigue crack in double-notch shear configuration in (a) $R = 0.1$ and (b) $R = 0.3$ compared with the experimental data [68].

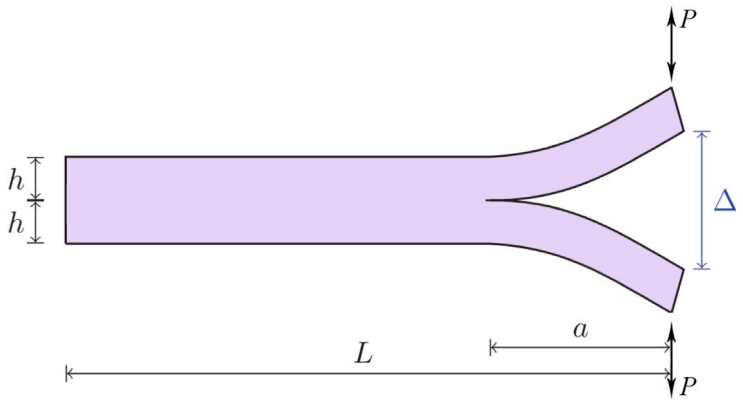

Fig. 11. Double Cantilever Beam (DCB) configuration within the crack propagation regime in pure mode I loading.

Table 3
Dimensions of the DCB, ENF and MMB specimens.

Test configuration	a [mm]	w [mm]	L [mm]	2h [mm]	C [mm]
DCB	50.8	25.4	110.8	4.5	–
ENF	25.4	25.1	101.6	4.5	–
MMB (50%)	28.8	25.4	101.6	4.5	41.3

3.3. Fatigue delamination damage propagation assessment

In order to investigate the crack propagation through the homogenization theory proposed herein, three standard test methods, i.e., Double Cantilever Beam (DCB), End Notch Flexure (ENF), and Mixed Mode Bending (MMB) are employed. The same material properties as in Section 3.2 are utilized, and an orthotropic material model has been used for describing the mechanical behavior of laminae within the classical mixing theory.

DCB test is simulated according to the extensive experimental procedure presented in [69]. The configuration is illustrated in Fig. 11 where two cyclic loads with the same characteristics are exerted on both flanges of the sample in opposite directions. In this way, the pre-cracked area is expected to grow in a pure tension mode. Table 3 summarizes the dimensions of the sample as well as the initial crack within the mid-plane of the specimen.

Crack propagation assessment requires the amount of the crack extension within the sample at regular time intervals. However, measuring the crack extent directly from the finite element model in the post-process could be time consuming and inefficient. To address this issue, an experimentally-measurable quantity could be employed as a reference, and the crack length will be obtained accordingly after a calibration process. For the DCB test, an analytical formulation based on the corrected beam theory has been presented to calculate the crack length, a, as a function of the specimen compliance, C, [42]:

$$a = \left(\frac{3}{2}C\ EI\right)^{\frac{1}{3}} - \chi h \tag{23}$$

in which

$$EI = E_{11}\frac{bh^3}{12} \tag{24}$$

$$\chi = \sqrt{\frac{E_{11}}{11G_{13}}\left[3 - 2\left(\frac{\Gamma}{1+\Gamma}\right)^2\right]} \tag{25}$$

where

$$\Gamma = 1.18\frac{\sqrt{E_{11}E_{22}}}{G_{13}} \tag{26}$$

being χ and Γ the crack length and transverse modulus correction parameters, respectively. Energy release rate in mode I loading (G_I) could also be calculated as a function of the reaction force (P) as well as the crack length as:

$$G_I = \frac{P^2(a+\chi h)^2}{wEI}. \tag{27}$$

According to the experimental procedure, the simulations are conducted in a displacement control mode where the maximum amounts of the displacement applied are $\delta = 1.48$ mm, 1.7 mm, 1.92 mm, *and* 2.25 mm, and the stress ratio is $R = 0.1$. Crack propagation rate (da/dN) is calculated utilizing the finite difference method according to Eq. (23). Fatigue crack extension rates versus the corresponding energy release rates are compared to the experimental values as illustrated in Fig. 12.

Arrows in Fig. 12 indicate the direction of the diagram as crack is propagated. Initially, fatigue crack propagates at high rates, which is attributed to the formation of a process zone as the result of a monotonic damage within the first cycle. The crack then reaches a stable condition in propagation which considers as the Paris law region. To reach a unified Paris law description among all simulations conducted, the point where 5 percent increase in compliance is detected would be considered in each load level, and a Paris law equation of the form

$$\frac{\mathrm{da}}{\mathrm{dN}} = m(G^{max})^n \tag{28}$$

is fitted through these points. In case of the DCB test, Paris law description is also included in Fig. 12 by considering 1.79 and 5.03 for m and n parameters, respectively. As it can be observed, the present model has the ability to predict mode I fatigue crack behavior in the propagation stage with an acceptable accuracy.

On the other hand, however, it seems to be necessary to investigate the fatigue crack propagation in mode two shear loading, since the model treats different modes in independent ways. Validating the numerical model in the shear mode would pave the way in applying the current formulation in more complex loading conditions and structures. ENF is considered as the standard test method to evaluate the current implementation. A schematic view of this test is presented in Fig. 13, while the dimensions are mentioned in Table 3. A cyclic displacement is applied at the center of the beam, and the two ends are modeled to be simply-supported.

As in the DCB test, ENF configuration is also accompanied by closed form solutions to calculate the crack extension and the energy release rate. Crack length could be calculated according to the instantaneous specimen compliance (C) as below [71]:

$$a = \left(\frac{96C\ EI - 2L^3}{3}\right)^{\frac{1}{3}} - 0.42\chi h \tag{29}$$

where EI and χ can be calculated from Eqs. (24) and (25), respectively. Mode II energy release rate then would be:

$$G_{II} = \frac{3(a+0.42\chi h)^2P^2}{64w\ EI} \tag{30}$$

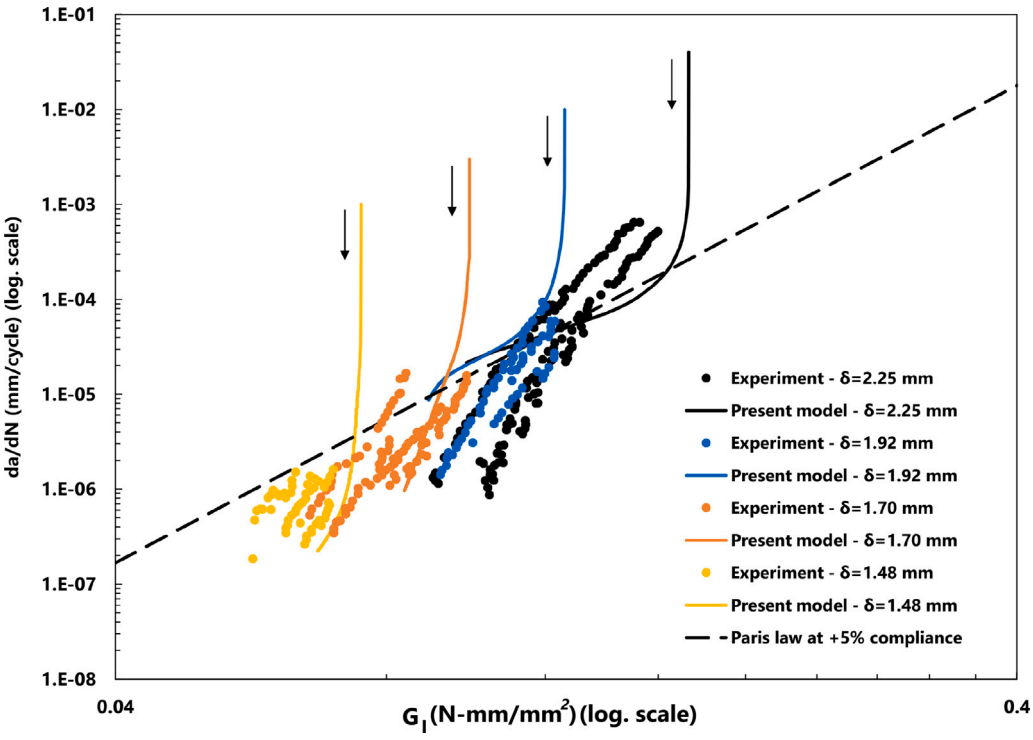

Fig. 12. Numerical results of the crack propagation within the DCB configuration compared to the experimental data [42,69,70].

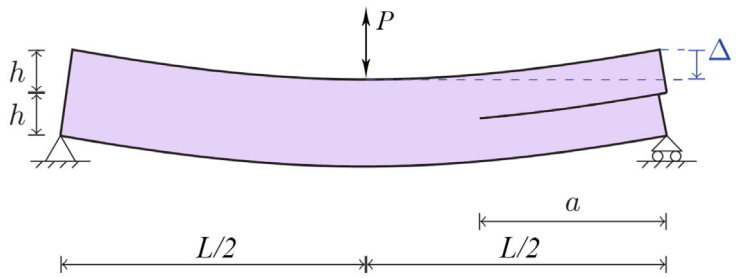

Fig. 13. End Notch Flexure (ENF) configuration within the crack propagation regime in pure mode II loading.

As opposed to the DCB configuration, ENF tests are conducted under load-control conditions at load levels of $P = 660.8$ N, 809.5 N, 931.7 N, *and* 1037.7 N with a stress ratio of $R = 0.1$. Crack propagation and energy release rates are calculated and compared to the experimental data [72] at each load level as shown in Fig. 14.

Comparing experimental and numerical values, a good agreement could be observed in terms of the energy release rate and crack extension characteristics. There are two drops in the crack propagation rates. The first one, which is observed in all loading levels at the beginning of the propagation stage, is due to the formation of the process zone whilst the second one, which could be noticed at Figs. 14(c) and 14(d) at the end of the propagation, is mainly due to the crack arrival to the center of the specimen, where stress conditions are changed according to the exerted central load at the crack tip vicinity. In order to have a unified response composed of all loading levels, points of 5 percent increment in specimen's compliance are obtained, and a Paris law in the form of Eq. (28) is fitted through these points, as illustrated in Fig. 15. Values of 0.30 and 2.93 are used for m and n parameters, respectively.

As it can be seen, although the numerically-obtained Paris law is within an acceptable range of the experimental values, there are some discrepancies, specifically at high crack propagation rates. This could be attributed to the main assumptions made once the homogenization theory has been employed. Indeed, the theory utilizes a combination of stresses of all layers according to their volumetric participation at the integration point level. This could lead to the loss of some data regarding the position of the layers, as it has been commented in [51]. The issue could be more pronounced in cases that there is a neutral axis within the sample, as in case of the ENF configuration, which can lead to some deviations from the experimental results.

A Mixed Mode Bending (MMB) test is considered to assess the present model within a combination of mode I and mode II loadings. The configuration is presented in Fig. 16(a), where a rigid lever is employed to exert certain amount of loading to the central and end part of the sample. The value of C parameter would specify the mode mix ratios within the fatigue tests. Dimensions of the MMB sample are mentioned in Table 3.

According to Fig. 16(b), the loading lever is eliminated in the simulations and two equivalent loads are considered. The proportion of these two loads determines the mode mix ratio of the problem as follows [12]:

$$\frac{P_1}{P_2} = \frac{c + \frac{L}{2}}{c}. \tag{31}$$

In current simulation, a value of 41.3 mm is chosen, which corresponds to a mode mixity of 50%. To obtain the crack length, a quadratic

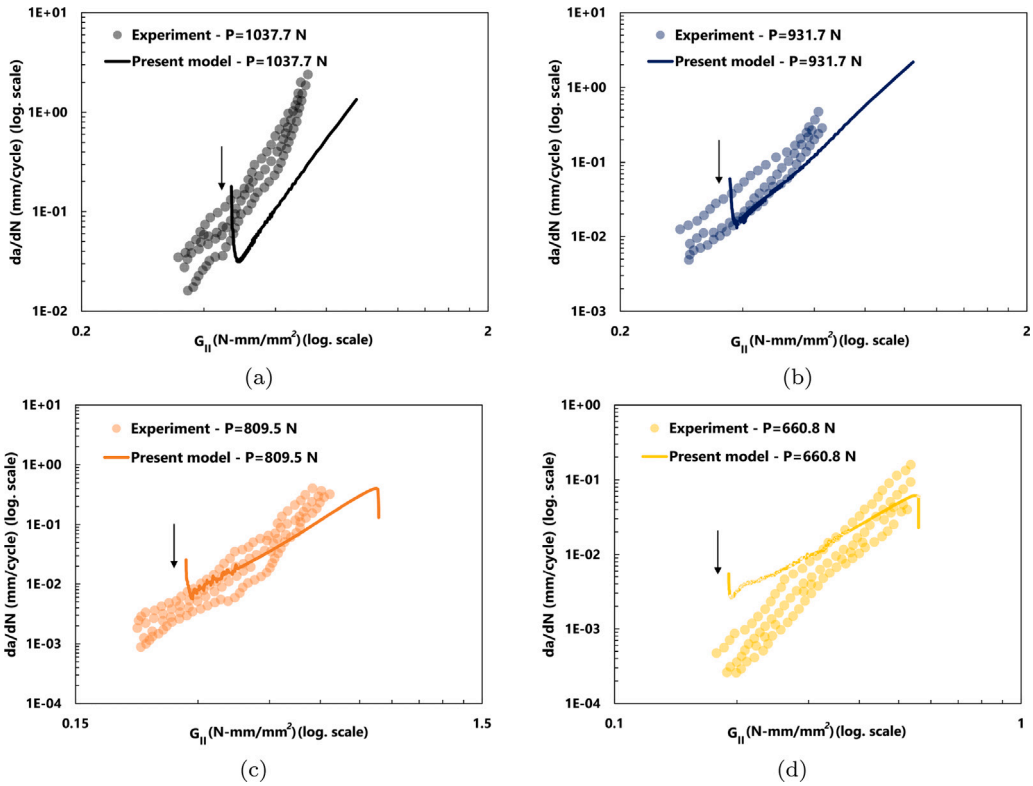

Fig. 14. Fatigue crack propagation in shear mode II at (a) $P = 1037.7$ N, (b) $P = 931.7$ N, (c) $P = 809.5$ N, and (d) $P = 660.8$ N compared to the experimental data [72].

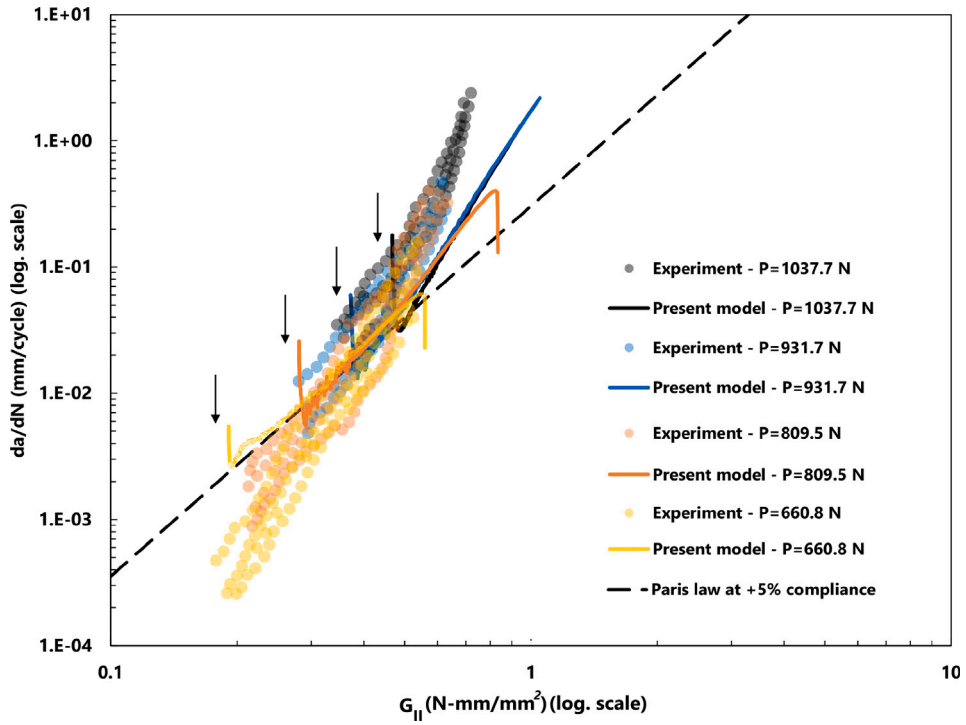

Fig. 15. Paris law fitted curve on the overall response in all the loading levels compared with the experimental results in loading mode II conditions [72].

polynominal has been presented in [42], which is used in the current study. For a specimen with 25.4 mm width, the crack length, a [mm], based on compliance, δ/P [mm/N], is:

$$a = -3.37 \cdot 10^5 \left(\frac{\delta}{P}\right)^2 + 8.55 \cdot 10^3 \left(\frac{\delta}{P}\right) - 1.572 \tag{32}$$

Load (P), and Load-point deflection (δ) are obtained as [12,51]:

$$P = \frac{L/2}{c + L/2} P_1 \tag{33}$$

$$\delta = \frac{2c + L}{L} \triangle_C - \frac{2c}{L} \triangle_E \tag{34}$$

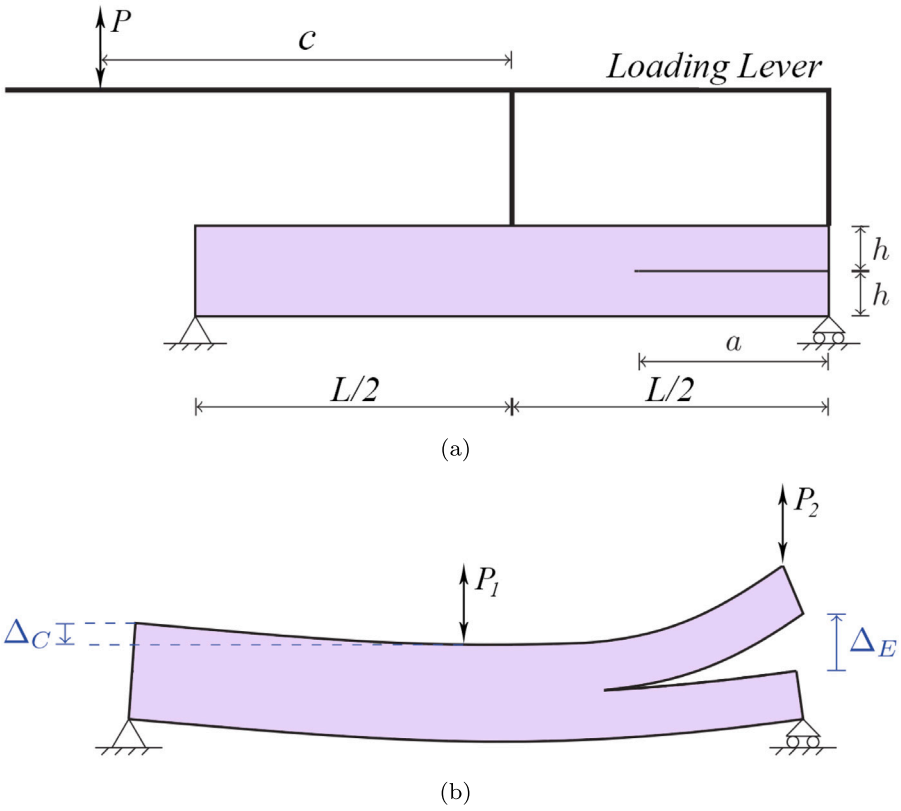

Fig. 16. Mixed Mode Bending (MMB) configuration within the crack propagation area in (a) real test conditions and (b) equivalent numerical configuration.

$\triangle_C$ and $\triangle_E$ being the central deflection and end opening as illustrated in Fig. 16(b). Mixed-mode energy release rate could be obtained using the following relation [71]:

$$G = \left[4\left(3c - \frac{L}{2}\right)^2 (a + \chi h)^2 + 3\,(c + L)^2\,(a + 0.42\chi h)^2\right] \cdot \frac{P^2}{64w\left(\frac{L}{2}\right)^2 EI_b} \tag{35}$$

in which

$$EI_b = \frac{4\left(3c - \frac{L}{2}\right)^2 (a + \chi h)^3 + \left(c + \frac{L}{2}\right)^2 \left[3\,(a + 0.42\chi h)^3 + 2\left(\frac{L}{2}\right)^3\right]}{96\left(\frac{L}{2}\right)^2 C} \tag{36}$$

Simulations are conducted in a load-control mode at three load levels of $P = 222$ N, $P = 193$ N, and $P = 170$ N, while maintaining the stress ratio to be $R = 0.1$. Simulation results are compared with the experimental values reported in [42] at the same mode mixity, as it is presented in Fig. 17.

Although a good correlation could be found between numerical and experimental results in high load levels, there is a deviation in smaller load domains, as it can bee observed in the case of $P = 170$ N, however, the simulation results still fall within an acceptable range of the experimental counterparts in terms of the rate of diagram evolution. The error could be attributed to the homogenization assumption, as it has been outlined for the ENF loading case. A Paris law curve of the form of Eq. (28) is fitted to the points of 5 percent increase in compliance with 0.11 and 2.47 for m and n parameters, respectively. A close examination of the obtained results would uncover the fact that there are some shifts in the experimental data to the right or left side of the fitted Paris law. As it is mentioned in [42], this could be improved by incorporating the R-curve effects, in which the critical energy release rate is increased as a function of the crack extension.

4. Conclusion

In the present study, a novel methodology was developed to simulate fatigue crack initiation and propagation within a homogenized medium. To this end, explicit representation of the bulk layers and interfaces were eliminated and their mechanical response was considered inside a rule of mixtures approach. Interfacial stresses were calculated based on the state of stress in the adjacent bulk layers. In addition to the damage under monotonic loads, the possibility of mechanical properties deterioration under cyclic loads was added to the homogenized formulation via a fatigue reduction function for each mode I and mode II loadings, independently. Conceptualization of this function was conducted in three distinct fatigue regions, i.e., sub-critical, critical, and over-critical stages, based on the stress level at each integration point. An advance-in-time strategy was added to the calculations to skip some cycles once a relative stability had been obtained in terms of the damage evolution.

Calibration of the model was conducted according to the Wöhler diagrams of mode I and mode II independently for unidirectional carbon/epoxy (IM7/8552) composite material. Three-point bending and double-notched shear tests were employed to assess the delamination initiation at different stress ratios. The results highlighted the capability of the present model in capturing the number of cycles to initiate a catastrophic crack formation within the model. On the other side, crack propagation was investigated through Double Cantilever beam (DCB), End Notch Flexure (ENF), and Mixed Mode Bending (MMB) tests for normal, shear, and mixed mode loading scenarios. Closed form equations were utilized in combination with the finite element solution to calculate fatigue crack extension on the basis of the specimen's

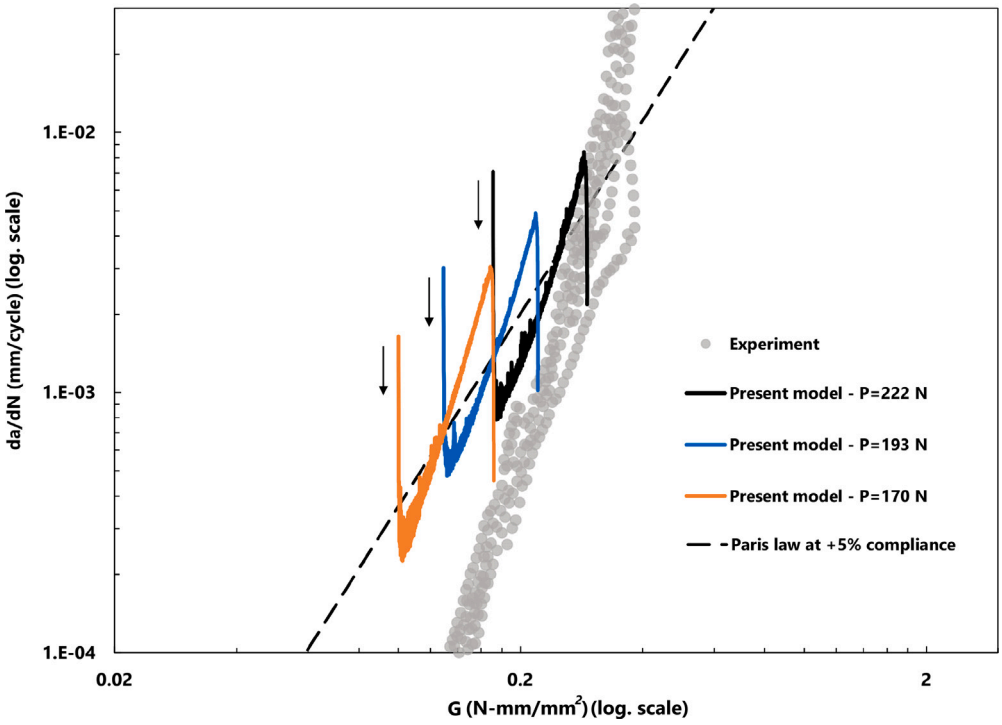

Fig. 17. Simulation results of the MMB configuration compared with the experimental data [42].

compliance. A good agreement was observed in the crack propagation behavior with respect to the experimental data, however, some discrepancies were detected specifically at low loading levels, which might be ascribed to the homogenization theory and the elimination of the explicit representation of the layers.

Utilizing virtual layers and interfaces makes the present model a highly favorable option for simulating large-scale structures with large number of layers. This also facilitates the pre-process stage as there will be no need to consider a layer-by-layer approach. In addition, calibrating the fatigue parameters using only one interface, the model would be able to take different orientations and stacking sequences into account. Although there would be some loss of accuracy according to the homogenization procedure, the present study demonstrated that this issue is not significant at the coupon level, which will pave the way of applying the method at the component level such as naval, automotive, or aerospace structures.

The model is compatible with any standard finite element code, and is currently implemented in the Kratos Multi-physics framework, which is accessible in an open-source platform.

CRediT authorship contribution statement

Alireza Taherzadeh-Fard: Writing – original draft, Software, Methodology, Investigation, Conceptualization. **Sergio Jiménez:** Writing – review & editing, Software. **Alejandro Cornejo:** Writing – review & editing, Software. **Eugenio Oñate:** Writing – review & editing, Supervision, Funding acquisition. **Lucia Gratiela Barbu:** Writing – review & editing, Supervision, Project administration, Funding acquisition.

Declaration of competing interest

The authors declare that they have no known competing financial interests or personal relationships that could have appeared to influence the work reported in this paper.

Data availability

Data will be made available on request.

Acknowledgement

The authors *Lucia Gratiela Barbu* and *Alejandro Cornejo* are Serra Húnter Fellows.

References

[1] Tsokanas P, Loutas T, Kotsinis G, Kostopoulos V, van den Brink WM, Martin de la Escalera F. On the fracture toughness of metal-composite adhesive joints with bending-extension coupling and residual thermal stresses effect. Composites B 2020;185:107694. http://dx.doi.org/10.1016/j.compositesb.2019.107694, URL https://www.sciencedirect.com/science/article/pii/S1359836819317548.

[2] Eliasson S, Hultgren G, Wennhage P, Barsoum Z. Numerical fatigue assessment of a cross-ply carbon fiber laminate using a probabilistic framework. Composites B 2024;281:111514. http://dx.doi.org/10.1016/j.compositesb.2024.111514, URL https://www.sciencedirect.com/science/article/pii/S1359836824003251.

[3] Zhou X-Y, Qian S-Y, Wang N-W, Xiong W, Wu W-Q. A review on stochastic multiscale analysis for FRP composite structures. Compos Struct 2022;284:115132. http://dx.doi.org/10.1016/j.compstruct.2021.115132, URL https://www.sciencedirect.com/science/article/pii/S026382232101549X.

[4] Granados JJ, Martinez X, Barbu LG, Di Capua D. Fatigue prediction of composite materials, based on serial/parallel mixing theory. Compos Struct 2022;291:115516. http://dx.doi.org/10.1016/j.compstruct.2022.115516, URL https://www.sciencedirect.com/science/article/pii/S0263822322003063.

[5] Nishi Y, Hosoi A, Kawada H. Evaluation of matrix crack growth in interlaminar toughened quasi-isotropic carbon-fiber reinforced plastic laminates up to the very-high cycle regime by ultrasonic fatigue testing. Compos Sci Technol 2024;253:110623. http://dx.doi.org/10.1016/j.compscitech.2024.110623, URL https://www.sciencedirect.com/science/article/pii/S0266353824001933.

[6] Kotrotsos A, Geitona A, Kostopoulos V. On the mode I and mode II fatigue delamination growth of CFRPs modified by electrospun bis-maleimide resin. Compos Sci Technol 2023;237:110000. http://dx.doi.org/10.1016/j.compscitech.2023.110000, URL https://www.sciencedirect.com/science/article/pii/S0266353823000933.

[7] Stoll MM, Weidenmann KA. Fatigue of fiber-metal-laminates with aluminum core, CFRP face sheets and elastomer interlayers (FMEL). Int J Fatigue 2018;107:110–8.

[8] Heidari-Rarani M, Sayedain M. Finite element modeling strategies for 2D and 3D delamination propagation in composite DCB specimens using VCCT, CZM and XFEM approaches. Theor Appl Fract Mech 2019;103:102246.

[9] Abdul Hamid ZM, Findeisen C, Laveuve DM, Rohrmüller B, Richter H, De Monte M, Spancken D, Hohe J. A continuum damage mechanics model for fatigue degradation and failure of short fiber reinforced composites. Compos Sci Technol 2024;110679. http://dx.doi.org/10.1016/j.compscitech.2024.110679, URL https://www.sciencedirect.com/science/article/pii/S0266353824002495.

[10] Zhao L, Zhi J, Zhang J, Liu Z, Hu N. XFEM simulation of delamination in composite laminates. Composites A 2016;80:61–71.

[11] Bak BL, Sarrado C, Turon A, Costa J. Delamination under fatigue loads in composite laminates: a review on the observed phenomenology and computational methods. Appl Mech Rev 2014;66(6):060803.

[12] Garg N, Prusty BG, Ooi ET, Song C, Pearce G, Phillips AW. Application of scaled boundary finite element method for delamination analysis of composite laminates using cohesive zone modelling. Compos Struct 2020;253:112773. http://dx.doi.org/10.1016/j.compstruct.2020.112773, URL https://www.sciencedirect.com/science/article/pii/S0263822320326994.

[13] Hu P, Li X, Lubineau G. Prediction of a complex delamination front using a general cohesive model. Compos Sci Technol 2023;233:109911. http://dx.doi.org/10.1016/j.compscitech.2023.109911, URL https://www.sciencedirect.com/science/article/pii/S0266353823000040.

[14] Zhu M, Gorbatikh L, Lomov SV. An incremental-onset model for fatigue delamination propagation in composite laminates. Compos Sci Technol 2020;200:108394. http://dx.doi.org/10.1016/j.compscitech.2020.108394, URL https://www.sciencedirect.com/science/article/pii/S0266353820321849.

[15] Carreras L, Bak B, Jensen S, Lequesne C, Xiong H, Lindgaard E. Benchmark test for mode I fatigue-driven delamination in GFRP composite laminates: Experimental results and simulation with the inter-laminar damage model implemented in SAMCEF. Composites B 2023;253:110529. http://dx.doi.org/10.1016/j.compositesb.2023.110529, URL https://www.sciencedirect.com/science/article/pii/S135983682300032X.

[16] Knopp A, Funck E, Holtz A, Scharr G. Delamination and compression-after-impact properties of z-pinned composite laminates reinforced with circumferentially notched z-pins. Compos Struct 2022;285:115188. http://dx.doi.org/10.1016/j.compstruct.2022.115188, URL https://www.sciencedirect.com/science/article/pii/S0263822322000058.

[17] Ye Q, Chen P. Prediction of the cohesive strength for numerically simulating composite delamination via CZM-based FEM. Composites B 2011;42(5):1076–83. http://dx.doi.org/10.1016/j.compositesb.2011.03.021, URL https://www.sciencedirect.com/science/article/pii/S1359836811001181.

[18] O'Brien TK, Chawan AD, Krueger R, Paris IL. Transverse tension fatigue life characterization through flexure testing of composite materials. Int J Fatigue 2002;24(2–4):127–45.

[19] Brod M, Dean A, Scheffler S, Gerendt C, Rolfes R. Numerical modeling and experimental validation of fatigue damage in cross-ply CFRP composites under inhomogeneous stress states. Composites B 2020;200:108050. http://dx.doi.org/10.1016/j.compositesb.2020.108050, URL https://www.sciencedirect.com/science/article/pii/S1359836820306624.

[20] Bak B, Turon A, Lindgaard E, Lund E. A benchmark study of simulation methods for high-cycle fatigue-driven delamination based on cohesive zone models. Compos Struct 2017;164:198–206.

[21] Maragoni L, Carraro PA, Simonetto M, Quaresimin M. A novel method to include crack-induced delamination in a fatigue damage predictive procedure for composite laminates. Compos Sci Technol 2023;238:110011. http://dx.doi.org/10.1016/j.compscitech.2023.110011, URL https://www.sciencedirect.com/science/article/pii/S0266353823001045.

[22] May M, Hallett SR. An advanced model for initiation and propagation of damage under fatigue loading – part I: Model formulation. Compos Struct 2011;93(9):2340–9. http://dx.doi.org/10.1016/j.compstruct.2011.03.022, URL https://www.sciencedirect.com/science/article/pii/S0263822311001061.

[23] May M, Hallett SR. A combined model for initiation and propagation of damage under fatigue loading for cohesive interface elements. Composites A 2010;41(12):1787–96. http://dx.doi.org/10.1016/j.compositesa.2010.08.015, URL https://www.sciencedirect.com/science/article/pii/S1359835X10002356.

[24] Rafiee R, Sotoudeh S. A hysteresis cohesive approach for predicting mixed-mode delamination onset of composite laminates under cyclic loading: Part I, model development. Compos Struct 2021;277:114667.

[25] Krueger R. Development of a benchmark example for delamination fatigue growth prediction. Fatigue Compos Mater 2010;3:54–73.

[26] Carloni C, Subramaniam KV. Investigation of sub-critical fatigue crack growth in FRP/concrete cohesive interface using digital image analysis. Composites B 2013;51:35–43. http://dx.doi.org/10.1016/j.compositesb.2013.02.015, URL https://www.sciencedirect.com/science/article/pii/S135983681300070X.

[27] Tang S, Lemanski S, Zhang X, Ayre D. Fatigue life prediction of z-fibre pinned composite laminate under mode I loading. Compos Sci Technol 2019;174:221–31. http://dx.doi.org/10.1016/j.compscitech.2019.02.010, URL https://www.sciencedirect.com/science/article/pii/S0266353818321249.

[28] Feng W, Arouche MM, Pavlovic M. Fatigue crack growth characterization of composite-to-steel bonded interface using ENF and 4ENF tests. Compos Struct 2024;334:117963. http://dx.doi.org/10.1016/j.compstruct.2024.117963, URL https://www.sciencedirect.com/science/article/pii/S0263822324000916.

[29] Tanulia V, Wang J, Pearce GM, Baker A, Chang P, Gangadhara Prusty B. Experimental and computational assessment of disbond growth and fatigue life of bonded joints and patch repairs for primary airframe structures. Int J Fatigue 2022;159:106776. http://dx.doi.org/10.1016/j.ijfatigue.2022.106776, URL https://www.sciencedirect.com/science/article/pii/S0142112322000561.

[30] Bender J, Bak B, Carreras L, Lindgaard E. Intralaminar crack growth rates of a glass fibre multiaxial laminate subjected to variable amplitude loading. Composites B 2023;252:110510. http://dx.doi.org/10.1016/j.compositesb.2023.110510, URL https://www.sciencedirect.com/science/article/pii/S1359836823000136.

[31] Zhang H, Qiao P. On the computation of energy release rates by a peridynamic virtual crack extension method. Comput Methods Appl Mech Engrg 2020;363:112883. http://dx.doi.org/10.1016/j.cma.2020.112883, URL https://www.sciencedirect.com/science/article/pii/S0045782520300657.

[32] Davis B, Wawrzynek P, Hwang C, Ingraffea A. Decomposition of 3-D mixed-mode energy release rates using the virtual crack extension method. Eng Fract Mech 2014;131:382–405. http://dx.doi.org/10.1016/j.engfracmech.2014.08.014, URL https://www.sciencedirect.com/science/article/pii/S0013794414002768.

[33] Farshidi A, Berggreen C, Schäuble R. Numerical fracture analysis and model validation for disbonded honeycomb core sandwich composites. Compos Struct 2019;210:231–8. http://dx.doi.org/10.1016/j.compstruct.2018.11.052, URL https://www.sciencedirect.com/science/article/pii/S0263822318322347.

[34] Zhou H, Li S, Xie K, Lu X, Zhao Y, Tay T. Mode II interlaminar fracture of hybrid woven carbon-dyneema composites. Composites A 2020;131:105785. http://dx.doi.org/10.1016/j.compositesa.2020.105785, URL https://www.sciencedirect.com/science/article/pii/S1359835X20300233.

[35] Turon A, Costa J, Camanho P, Dávila C. Simulation of delamination in composites under high-cycle fatigue. Composites A 2007;38(11):2270–82. http://dx.doi.org/10.1016/j.compositesa.2006.11.009, URL https://www.sciencedirect.com/science/article/pii/S1359835X0600337X, CompTest 2006.

[36] May M, Hallett SR. An advanced model for initiation and propagation of damage under fatigue loading–part I: Model formulation. Compos Struct 2011;93(9):2340–9.

[37] May M, Pullin R, Eaton M, Featherston C, Hallett SR. An advanced model for initiation and propagation of damage under fatigue loading–part II: Matrix cracking validation cases. Compos Struct 2011;93(9):2350–7.

[38] Zhao M, Zhao Y, Wang A, Chang Z, Zhang J, Wang Z. Investigation of the mode-I delamination behavior of double-double laminate carbon fiber reinforced composite. Compos Sci Technol 2024;248:110463. http://dx.doi.org/10.1016/j.compscitech.2024.110463, URL https://www.sciencedirect.com/science/article/pii/S0266353824000332.

[39] Tao C, Qiu J, Yao W, Ji H. A novel method for fatigue delamination simulation in composite laminates. Compos Sci Technol 2016;128:104–15. http://dx.doi.org/10.1016/j.compscitech.2016.03.016, URL https://www.sciencedirect.com/science/article/pii/S026635381630104X.

[40] Springer M, Turon A, Pettermann H. A thermo–mechanical cyclic cohesive zone model for variable amplitude loading and mixed–mode behavior. Int J Solids Struct 2019;159:257–71. http://dx.doi.org/10.1016/j.ijsolstr.2018.10.004, URL https://www.sciencedirect.com/science/article/pii/S0020768318303986.

[41] Roth S, Kuna M. Prediction of size-dependent fatigue failure modes by means of a cyclic cohesive zone model. Int J Fatigue 2017;100:58–67. http://dx.doi.org/10.1016/j.ijfatigue.2017.01.044, URL https://www.sciencedirect.com/science/article/pii/S0142112317300531.

[42] Dávila C. From S-N to the Paris law with a new mixed-mode cohesive fatigue model for delamination in composites. Theor Appl Fract Mech 2020;106:102499. http://dx.doi.org/10.1016/j.tafmec.2020.102499, URL https://www.sciencedirect.com/science/article/pii/S0167844219305579.

[43] Falcó O, Ávila R, Tijs B, Lopes C. Modelling and simulation methodology for unidirectional composite laminates in a virtual test lab framework. Compos Struct 2018;190:137–59. http://dx.doi.org/10.1016/j.compstruct.2018.02.016, URL https://www.sciencedirect.com/science/article/pii/S0263822317329768.

[44] Settgast RR, Rashid MM. Continuum coupled cohesive zone elements for analysis of fracture in solid bodies. Eng Fract Mech 2009;76(11):1614–35.

[45] Roy P, Deepu S, Pathrikar A, Roy D, Reddy J. Phase field based peridynamics damage model for delamination of composite structures. Compos Struct 2017;180:972–93.

[46] Reinoso J, Blázquez A, Távara L, París F, Arellano C. Damage tolerance of composite runout panels under tensile loading. Composites B 2016;96:79–93. http://dx.doi.org/10.1016/j.compositesb.2016.03.083, URL https://www.sciencedirect.com/science/article/pii/S1359836816301743.

[47] Oller S, Salomón O, Oñate E. A continuum mechanics model for mechanical fatigue analysis. Comput Mater Sci 2005;32(2):175–95. http://dx.doi.org/10.1016/j.commatsci.2004.08.001, URL https://www.sciencedirect.com/science/article/pii/S0927025604001958.

[48] Barbu LG, Oller S, Martinez X, Barbat AH. High-cycle fatigue constitutive model and a load-advance strategy for the analysis of unidirectional fiber reinforced composites subjected to longitudinal loads. Compos Struct 2019;220:622–41. http://dx.doi.org/10.1016/j.compstruct.2019.04.015, URL https://www.sciencedirect.com/science/article/pii/S0263822318336481.

[49] Jiménez S, Barbu LG, Oller S, Cornejo A. On the numerical study of fatigue process in rail heads by means of an isotropic damage based high-cycle fatigue constitutive law. Eng Fail Anal 2022;131:105915. http://dx.doi.org/10.1016/j.engfailanal.2021.105915, URL https://www.sciencedirect.com/science/article/pii/S1350630721007767.

[50] Gonçalves LA, Jiménez S, Cornejo A, Barbu L, Parareda S, Casellas D. Numerical simulation of a rapid fatigue test of high Mn-TWIP steel via a high cycle fatigue constitutive law. Int J Fatigue 2023;168:107444. http://dx.doi.org/10.1016/j.ijfatigue.2022.107444, URL https://www.sciencedirect.com/science/article/pii/S0142112322006946.

[51] Taherzadeh-Fard A, Cornejo A, Jiménez S, Barbu LG. A rule of mixtures approach for delamination damage analysis in composite materials. Compos Sci Technol 2023;242:110160. http://dx.doi.org/10.1016/j.compscitech.2023.110160, URL https://www.sciencedirect.com/science/article/pii/S0266353823002531.

[52] Truesdell C, Toupin R. The classical field theories. In: Principles of classical mechanics and field theory/prinzipien der klassischen mechanik und feldtheorie. Springer; 1960, p. 226–858.

[53] Cornejo Velázquez A. A fully Lagrangian formulation for fluid-structure interaction between free-surface flows and multi-fracturing solids and structures (Thesis), 2020.

[54] Car E, Oller S, Oñate E. An anisotropic elastoplastic constitutive model for large strain analysis of fiber reinforced composite materials. Comput Methods Appl Mech Engrg 2000;185(2):245–77. http://dx.doi.org/10.1016/S0045-7825(99)00262-5, URL https://www.sciencedirect.com/science/article/pii/S0045782599002625.

[55] Balzani C, Wagner W. An interface element for the simulation of delamination in unidirectional fiber-reinforced composite laminates. Eng Fract Mech 2008;75(9):2597–615.

[56] Gonçalves LA, Jiménez S, Cornejo A, Tedesco MM, Barbu LG. A high cycle fatigue numerical framework for component-level virtual fatigue testing: Application to a light-duty vehicle lower control arm. Eng Struct 2024;311:118198.

[57] Alcayde B, Merzkirch M, Cornejo A, Jiménez S, Marklund E, Barbu L. Fatigue behaviour of glass-fibre-reinforced polymers: Numerical and experimental characterisation. Compos Struct 2024;337:118057. http://dx.doi.org/10.1016/j.compstruct.2024.118057, URL https://www.sciencedirect.com/science/article/pii/S0263822324001855.

[58] Dávila CG, Joosten MW. A cohesive fatigue model for composite delamination based on a new material characterization procedure for the Paris law. Eng Fract Mech 2023;284:109232.

[59] Dávila CG. From SN to the Paris law with a new mixed-mode cohesive fatigue model. Tech. rep., 2018.

[60] The MathWorks, Inc. MATLAB R2013a (8.1.0.604). Natick, Massachusetts, USA; 2013, Software.

[61] Maiti S, Geubelle PH. A cohesive model for fatigue failure of polymers. Eng Fract Mech 2005;72(5):691–708.

[62] Oller S. Nonlinear dynamics of structures. Springer; 2014.

[63] Barbu LG, Oller S, Martinez X, Barbat A. High cycle fatigue simulation: A new stepwise load-advancing strategy. Eng Struct 2015;97:118–29. http://dx.doi.org/10.1016/j.engstruct.2015.04.012, URL https://www.sciencedirect.com/science/article/pii/S0141029615002527.

[64] Ferrándiz VM, Bucher P, Rossi R, Cotela J, Carbonell J, Zorrilla R, Tosi R. KratosMultiphysics (version 8.0). 2020.

[65] Dadvand P, Rossi R, Oñate E. An object-oriented environment for developing finite element codes for multi-disciplinary applications. Arch Comput Methods Eng 2010;17:253–97.

[66] Ribó R, Pasenau M, Escolano E. GiD user manual. CIMNE; 2007.

[67] Dávila CG, Rose CA, Murri GB, Jackson WC, Johnston WM. Evaluation of fatigue damage accumulation functions for delamination initiation and propagation. Tech. rep., 2020.

[68] May M, Hallett SR. An assessment of through-thickness shear tests for initiation of fatigue failure. Composites A 2010;41(11):1570–8.

[69] Murri GB. Evaluation of delamination onset and growth characterization methods under mode I fatigue loading. Tech. rep., 2013.

[70] Nojavan S, Schesser D, Yang Q. An in situ fatigue-CZM for unified crack initiation and propagation in composites under cyclic loading. Compos Struct 2016;146:34–49.

[71] Reeder JR, Demarco K, Whitley KS. The use of doubler reinforcement in delamination toughness testing. Composites A 2004;35(11):1337–44.

[72] O'Brien TK, Johnston WM, Toland GJ. Mode II interlaminar fracture toughness and fatigue characterization of a graphite epoxy composite material. Tech. rep., 2010.